DOE/ET-53088-146 IFSR #146

THEORY OF RESISTIVITY-GRADIENT-DRIVEN TURBULENCE

L. Garcia and B. A. Carreras
Oak Ridge National Laboratory

P. H. Diamond
Institute for Fusion Studies

J. D. Callen
University of Wisconsin

October 1984

146

THEORY OF RESISTIVITY-GRADIENT-DRIVEN TURBULENCE[a)]

L. Garcia, P. H. Diamond[b)], B. A. Carreras, and J. D. Callen[c)]

Oak Ridge National Laboratory, Oak Ridge, Tennessee 37831

ABSTRACT

A theory of the nonlinear evolution and saturation of resistivity-driven turbulence, which evolves from linear rippling instabilities, is presented. The nonlinear saturation mechanism is identified both analytically and numerically. Saturation occurs when the turbulent diffusion of the resistivity is large enough so that dissipation due to parallel electron thermal conduction balances the nonlinearly modified resistivity gradient driving term. The levels of potential, resistivity, and density fluctuations at saturation are calculated. A combination of computational modeling and analytic treatment is used in this investigation.

---

a)Research sponsored by the Office of Fusion Energy, U.S. Department of Energy, under Contract No. DE-AC05-84OR21400 with Martin Marietta Energy Systems, Inc.

b)Permanent address: Institute for Fusion Studies, University of Texas, Austin, Texas 78712.

c)Permanent address: University of Wisconsin, Madison, Wisconsin 53706.

I. INTRODUCTION

Tokamak edge plasmas exhibit turbulence characterized by large density and electrostatic potential fluctuations[1,2] in regions of significant cross-field transport. It is important to develop an understanding of the observed fluctuations and transport in order to optimize design of divertors and limiters and in order to gain insight into the effects of the edge turbulence on improved tokamak operation regimes, such as the ASDEX H-mode,[3] and on edge pumping schemes. Also, since the edge turbulence is strong and relatively well diagnosed experimentally, it provides an excellent test bed for the development of realistic and comprehensive nonlinear plasma turbulence models.

Turbulence driven by resistivity gradients, via mechanisms such as the rippling mode,[4] has been advanced as a possible explanation for the edge fluctuations and anomalous transport. Previous investigations have discussed the linear and quasi-linear theory of rippling modes,[5] an elementary theory of the initial transition to nonlinear evolution,[6] and the viability of rippling modes as an explanation of experimentally observed edge turbulence in tokamaks.[6] In this paper, a theory of the nonlinear evolution and saturation of resistivity-gradient-driven turbulence, which evolves from linear rippling instabilities, is presented. The nonlinear saturation mechanism is identified, and the characteristics of steady-state, resistivity-gradient-driven turbulence are discussed. The levels of potential, resistivity, and density fluctuations and of energy and particle transport are calculated. Throughout the paper, theoretical assumptions and predictions are

examined in detail and compared to the numerical solutions of the basic nonlinear equations.

Rippling modes are primarily electrostatic instabilities that result from the coupling of resistivity fluctuations to potential and current fluctuations through Ohm's law. The resistivity fluctuations are driven by convective relaxation of the average temperature gradient. In addition to resistive field line diffusion, parallel thermal conduction $\chi_{\parallel}\nabla_{\parallel}^2$, which restricts the resistivity response to a small region about the mode resonance surface, is a strong stabilizing effect. Thus, rippling modes are not generally thought to be an important instability mechanism in regimes of moderate $\chi_{\parallel}$.

However, in this paper, it is shown that nonlinearly evolving resistivity-gradient-driven turbulence departs significantly from expectations based on the linear theory of the rippling mode. Indeed, this departure is the motivation for the distinction, made frequently in the course of this paper, between (linear) rippling instabilities and resistivity-gradient-driven turbulence. Here, the theory of stationary resistivity-gradient-driven turbulence is cast in a simple framework similar to that used to describe turbulent hydrodynamic shear flows; namely, saturation by the (nonlinear) dynamically regulated balance of energy input by gradient relaxation with dissipation. In particular:

(i) Using the numerical solutions, the efficiency of the nonlinear saturation mechanism for a fixed average resistivity profile $\eta_0(r)$, the case relevant to experiment, and its importance relative to quasi-linear flattening of $d\eta_0/dr$ are verified in detail.

(ii) The radial asymmetry and nonlinear broadening of the resistivity and potential eigenfunctions imply that, in the region where resistivity-gradient-free energy is extracted, the perturbed current $\tilde{J}_z \approx 0$. As a consequence, the vorticity evolution decouples from the resistivity evolution. The nonlinear dynamics are governed by the nonlinear resistivity evolution equation and Ohm's law, now simplified to $-\nabla_{\parallel}\phi \approx \tilde{\eta}J_{z0}$.

(iii) As a result of the interaction of turbulent radial diffusion and parallel thermal conduction, the nonlinearly evolving resistivity and potential eigenfunctions are characterized by an amplitude-dependent radial scale length[6] $\Delta^c = (D/\chi_{\parallel}k_{\parallel}'^2)^{1/4}$, where D is the turbulent diffusion cofficient and $k_{\parallel}'$ is the radial derivative of the parallel wave vector.

(iv) At saturation, the level of diffusion and thus the mixing length Δ^c adjust to a value at which thermal dissipation balances resistivity gradient drive. This result supersedes our previous work,[5] in which the fluctuation level at which transition to nonlinear evolution occurs was calculated using a linear rather than a nonlinear drive.

Points (i) through (iv) are the principal results presented in this paper that pertain to the basic physics of resistivity-gradient-driven turbulence. Due to the simplicity of the rippling mode model, it is reasonable to expect that the nonlinear evolution of many other dynamical systems may exhibit features similar to those discussed here. Thus, these results may be of general interest.

In addition to the elucidation of the basic nonlinear physics, this paper discusses the analytical and numerical calculation of several relevant physical quantities. The root-mean-square (rms) potential fluctuation level $(e\phi/T_e)_{rms}$ and resistivity fluctuation level $(\tilde{\eta}/\eta_0)_{rms}$ are predicted. Treating the density as a passive scalar convected by fluid turbulence, a density fluctuation level $(\tilde{n}/n_0)_{rms}$ is estimated. For parameters similar to those of Macrotor edge plasmas, a density fluctuation level $(\tilde{n}/n_0)_{rms} \approx 0.24$ is predicted with the corresponding temperature fluctuation level being $(\tilde{T}/T_0)_{rms} \approx 0.05$. The induced anomalous particle and thermal transport is also discussed.

The remainder of the paper is organized in the following manner. The basic resistivity-gradient-driven turbulence model is presented in Sec. II. In Sec. III, the dynamics of nonlinear evolution and saturation are described. The nonlinear instability dynamics, the saturation mechanism, and the significance of the nonlinear resistivity mixing length are all discussed in detail. Section IV contains a discussion of the results of multiple-helicity nonlinear numerical calculations. Questions of numerical convergence and the relative

importance of nonlinear saturation and quasi-linear profile flattening are also addressed there. In Sec. V, predicted fluctuation and transport levels are presented. Section VI contains the summary and conclusions.

II. RESISTIVITY-GRADIENT-DRIVEN TURBULENCE MODEL

In this section, the basic resistivity-gradient-driven turbulence model is presented and discussed. A simplified set of nonlinear equations that describe the nonlinear evolution and saturation of electrostatic rippling instabilities is derived, and quadratic energy-like quantities are identified.

The reduced resistive magnetohydrodynamic (MHD) equations in cylindrical geometry[7] are

$$E_{\parallel} = \frac{\partial \psi}{\partial t} - B_z \nabla_{\parallel} \phi = \eta J_z \ , \tag{1}$$

$$\frac{dU}{dt} = B_z \nabla_{\parallel} J_z \ , \tag{2}$$

where ψ is the poloidal flux function, ϕ is the fluid stream function ($= \Phi/B$, where Φ is the electrostatic potential),

$$J_z = \frac{1}{\mu_0} \nabla_{\perp}^2 \psi$$

is the current, and

$$U = \vec{\nabla}_{\perp} \cdot (\rho_m \vec{\nabla}_{\perp} \phi)$$

is the component of the vorticity in the z-direction. The coordinate z is taken to extend along the axis of the cylinder. Here ρ_m is the mass density. In Eqs. (1) and (2),

$$\frac{d}{dt} \equiv \frac{\partial}{\partial t} + (\vec{\nabla}_\perp \phi \times \hat{z}) \cdot \vec{\nabla}$$

and

$$B_z \nabla_\parallel \equiv (\vec{\nabla}_\perp \psi \times \hat{z}) \cdot \vec{\nabla} + B_z \frac{\partial}{\partial z}$$

are the total convective derivative and the parallel gradient, respectively. To describe rippling instabilities, a resistivity evolution (thermal balance) equation is necessary.[4] In its simplest form, this equation is

$$\frac{d\eta}{dt} = \nabla_\parallel (\chi_\parallel \nabla_\parallel \eta) \quad . \tag{3}$$

Here $\chi_\parallel$ is the parallel electron heat conductivity. Equations (1)-(3) constitute the basic resistivity-gradient-driven turbulence model. These are the equations used in the numerical calculations.[8]

Significant simplification of the basic model can be achieved by using the electrostatic approximation, whereby $\tilde{\psi} = 0$ and $\nabla_\parallel = \nabla_\parallel^{(0)} = \hat{b} \cdot \vec{\nabla}$. The vector $\hat{b}$ is a unit vector parallel to the equilibrium magnetic field. The validity of this approximation in the context of rippling instabilities was discussed in Ref. 6. Employing the electrostatic approximation and writing J_z and η as a sum of average (slowly varying) and perturbed (rapidly varying) pieces, Eqs. (1)-(3) can be simplified to

$$-B_z \nabla_\parallel^{(0)} \phi = \tilde{\eta} J_{z0} + \eta_0 \tilde{J}_z \quad , \tag{4}$$

$$\rho_m \frac{d}{dt} \nabla_\perp^2 \phi = B_z \nabla_\parallel^{(0)} \tilde{J}_z \ , \tag{5}$$

$$\frac{d\tilde{\eta}}{dt} - \chi_\parallel \nabla_\parallel^{(0)2} \tilde{\eta} = -\frac{1}{r} \frac{\partial \phi}{\partial \theta} \frac{d\eta_0}{dr} \ . \tag{6}$$

The subscript 0 is used to indicate average quantities and the tilde ($\sim$) to indicate perturbed ones. As a consequence of the electrostatic approximation, Ohm's law [Eq. (4)] has been linearized. As a result, the current perturbation $\tilde{J}_z$ can now be eliminated from Eq. (5), yielding two nonlinear equations for ϕ and $\tilde{\eta}$,

$$\frac{\rho_m}{B_z^2} \frac{d}{dt} \nabla_\perp^2 \phi = -\frac{1}{\eta_0} \nabla_\parallel^{(0)2} \phi - \frac{J_{z0}}{B_z} \nabla_\parallel^{(0)} \left(\frac{\tilde{\eta}}{\eta_0} \right) , \tag{7}$$

$$\frac{d}{dt} \tilde{\eta} - \chi_\parallel \nabla_\parallel^{(0)2} \tilde{\eta} = -\frac{1}{r} \frac{\partial \phi}{\partial \theta} \frac{d\eta_0}{dr} \ . \tag{8}$$

Equations (7) and (8), for the vorticity and resistivity respectively, constitute the basic resistivity-gradient-driven turbulence model to be used in the analytic calculations.

The linear instability regime described by Eqs. (7) and (8) has been studied in detail in Ref. 5. The basic results are that this system of equations reduces, in the linear approximation, to a single second-order equation,

$$\frac{d^2\phi}{dX^2} - \left(\frac{1}{4} X^2 - \delta \frac{X}{1 + bX^2} \right) \phi = 0 \ ,$$

where $X = x/x_R$ is the radial variable that is dedimensionalized in terms of a resistive singular layer width x_R with

$$x_R = \left[\gamma \left(\frac{\mu_0 \rho_m}{B_z^2}\right) \frac{\eta_0(r_s)}{\mu_0} \frac{L_s^2 r_s^2}{4m^2}\right]^{1/4} ,$$

$$\delta = -\frac{L_s}{L_\eta} \frac{\eta_0 J_{z0}}{B_z}\bigg|_{r_s} \frac{1}{2\gamma x_R} ,$$

$$b = \frac{m^2}{r_s^2 L_s^2} \chi_{\parallel} \frac{x_R^2}{\gamma} .$$

Here, $L_\eta = [d(\ln \eta_0)/dr]^{-1}$ is the gradient scale length of the resistivity, and $L_s = (r_s q'/R_0 q^2)^{-1}$ is the magnetic shear scale length. A key dimensionless ratio is $S = \tau_R/\tau_{Hp}$, where $\tau_R = \mu_0 a^2/\eta_0$ is the resistive diffusion time scale, and $\tau_{Hp} = R_0/V_A$ is the poloidal hydromagnetic time with $V_A = B_z/(\mu_0 \rho_m)^{1/2}$ the Alfven speed.

In the absence of parallel electron heat conduction ($b = 0$), the lowest-order eigenmode is

$$\phi = \phi_0 \exp\left[-\frac{(X - \delta)^2}{4}\right] \exp\left[-i\left(\frac{n}{R_0} z - m\theta\right) + \gamma t\right]$$

with eigenvalue $\delta = \sqrt{2}$ and, hence,

$$\gamma = \left[\frac{Sm L_s \eta_0 (r_s)^2 J_{z0}(r_s)^2}{4 r_s L_\eta^2 B_z^2}\right]^{2/5} \tau_R^{-1} .$$

In the limit of large electron heat conduction,[5,9] the linear growth rate is

$$\gamma = 5.8\left[\frac{\eta_0(r_s)}{\mu_0\chi_{\parallel}}\right]^{4/3}\left[\frac{L_s^3 r_s}{L_\eta^2}\frac{\eta_0(r_s)J_{z0}(r_s)}{mB_z}\right]^{2/3} S^2 \ .$$

Note that parallel electron heat conduction reduces the growth rate for $\chi_{\parallel} > \eta_0/\mu_0$ but does not completely stabilize the rippling modes because the $\chi_{\parallel}$ effects are negligible near $x = 0$.

It is straightforward to identify two energy-like quantities quadratic in the fluctuation level,

$$E_K = \frac{1}{2}\int d^3x \ |\vec{\nabla}_\perp\phi|^2 \ ,$$

$$E_T = \frac{1}{2}\int d^3x \ |\tilde{\eta}|^2 \ ,$$

for Eqs. (7) and (8), respectively. These quantities satisfy the evolution equations

$$\frac{\partial E_K}{\partial t} = \frac{B_z^2}{\rho_m}\int d^3x\left[\frac{\phi^* J_{z0}}{B_z}\nabla_{\parallel}^{(0)}\left(\frac{\tilde{\eta}}{\eta_0}\right) - \frac{|\nabla_{\parallel}^{(0)}\phi|^2}{\eta_0}\right] , \tag{9}$$

$$\frac{\partial E_T}{\partial t} = \int d^3x \left[-\tilde{\eta}^* \frac{1}{r}\frac{\partial\phi}{\partial\theta}\frac{d\eta_0}{dr} - \chi_{\parallel}|\nabla_{\parallel}^{(0)}\tilde{\eta}|^2\right] . \tag{10}$$

Equation (9) states that E_K, the fluid kinetic energy, evolves by a

competition between a destabilizing $\vec{J} \times \vec{B}$ force induced by resistivity perturbations and a stabilizing $\vec{J} \times \vec{B}$ force induced by the magnetic field line diffusion. Similarly, Eq. (10) states that E_T, indicative of the mean-square resistivity fluctuation level, is driven by relaxation of the average resistivity gradient [note that $\langle(\tilde{\eta}/r)\ (\partial\phi/\partial\theta)\rangle$ is the average radial resistivity flux] and damped by dissipation due to $\chi_{\parallel}$.

III. DYNAMICS OF NONLINEAR EVOLUTION AND SATURATION

In this section, the analytic theory of nonlinear evolution and saturation of resistivity-gradient-driven turbulence is presented. The level of resistivity diffusion at saturation is calculated. The implications of these results for predictions of experimentally observable fluctuation levels and edge transport are then discussed in Sec. V.

Before proceeding with our discussion of the dynamics of nonlinear evolution and saturation of resistivity-gradient-driven turbulence, we pause to address the question of whether quasi-linear flattening of $d\eta_0/dr$ or turbulent stabilization is the relevant saturation mechanism. First, in the relevant case of turbulence in tokamaks, the average temperature (and thus the resistivity) gradient is maintained by the balance of ohmic heating with thermal transport. Thus, a nonlinear, rather than quasi-linear, saturation mechanism is necessary for a theory of steady-state, fixed resistivity-gradient-driven turbulence. Second, in the relevant regime of large $\chi_{\parallel}$, the processes of radial diffusion and radially dependent parallel thermal conduction combine to produce an efficient nonlinear saturation mechanism, which persists in the presence of quasi-linear relaxation of $d\eta_0/dr$. The importance of this mechanism, described in detail in this section, can be illustrated by the heuristic argument that diffusion of $\tilde{\eta}$ couples to (diffusive) dissipation associated with $\chi_{\parallel}$ via the radial dependence of $k_{\parallel}$, but diffusion of η_0 cannot. Hence, it is not unreasonable that the nonlinear mechanism is more potent than quasi-linear flattening.

It is natural to specify the saturation condition for the resistivity-gradient-driven turbulence as

$$\frac{\partial E_K}{\partial t} = \frac{\partial E_T}{\partial t} = 0 \ ,$$

namely, that the turbulent energies must be stationary in time. Note that when this criterion is satisfied, resistive field line diffusion balances resistivity-induced destabilization in Eq. (9), and drive by $d\eta_0/dr$ relaxation balances dissipation due to $\chi_{\parallel}$ in Eq. (10).

It should be noted that requiring $\partial E_K/\partial t = 0$ is equivalent to imposing the criterion that

$$\int d^3x \ \phi^* \nabla_{\parallel}^{(0)} \tilde{J}_z = 0 \ .$$

A sufficient, but not necessary, condition for satisfying this criterion is that $\tilde{J}_z = 0$, leaving $\partial E_T/\partial t = 0$ with $-\nabla_{\parallel}^{(0)}\phi = \tilde{\eta} J_{z0}$ as the conditions used to determine the turbulence level at saturation. The condition $\tilde{J}_z = 0$ is satisfied except in the immediate vicinity of the mode rational surface ($x \approx 0$), where $\nabla_{\parallel}^{(0)}\phi \approx 0$ and $\tilde{\eta} J_{z0} \approx -\eta_0 \tilde{J}_z$. However, in this region $\phi^* \nabla_{\parallel}^{(0)} \tilde{J}_z \approx 0$ since $\nabla_{\parallel}^{(0)} \tilde{J}_z \approx 0$. Furthermore, the $\tilde{\eta}$ and ϕ eigenfunctions, which, in linear theory, are skewed off symmetry about the mode resonance surface, are broadened by turbulent diffusion as the fluctuation level increases. Thus, the detailed structure around $x = 0$ is smeared out. For these reasons, the region located at the singular surface is irrelevant to the nonlinear dynamics of rippling mode turbulence.

As a consequence of the saturation condition $\tilde{J}_z = 0$, the vorticity equation [Eq. (5)] decouples from Eqs. (4) and (6), which now exclusively determine the nonlinear evolution of the rippling modes. It is apparent that the structure of the resistivity perturbation is determined by the parallel electron thermal conduction term $-\chi_{\parallel}\nabla_{\parallel}^{(0)2}$ and the convective nonlinearity.

As discussed in Ref. 10, standard iterative methods can be used to obtain the renormalized resistivity evolution equation. The nonlinear resistivity evolution equation is

$$\frac{\partial\tilde{\eta}_{\vec{k}}}{\partial t} + \chi_{\parallel}k_{\parallel}^2\tilde{\eta}_{\vec{k}} + \left(\left\{\frac{\partial}{\partial x}\left[\sum_{\vec{k}'}(-ik_{\theta}')\phi_{-\vec{k}'}\tilde{\eta}_{\vec{k}''}\right] - ik_{\theta}\sum_{\vec{k}'}\frac{\partial\phi_{-\vec{k}'}}{\partial x'}\tilde{\eta}_{\vec{k}''}\right\}\right.$$

$$\left. - \left\{\frac{\partial}{\partial x}\left[\sum_{\vec{k}'}(-ik_{\theta}')\tilde{\eta}_{-\vec{k}'}\phi_{\vec{k}''}\right] - ik_{\theta}\sum_{\vec{k}'}\frac{\partial\tilde{\eta}_{-\vec{k}'}}{\partial x'}\phi_{\vec{k}''}\right\}\right) = -ik_{\theta}\phi_{\vec{k}}\frac{d\eta_0}{dr},$$

where all fields are expanded in toroidal and poloidal harmonics m, n. For simplicity, each harmonic is labeled with $\vec{k} = (m, n)$, and the following notation is used: $k_{\theta} = m/r$, $k_{\parallel} = [m/q(r) - n]/R_0$, $x = r - r_{\vec{k}}$, with $r_{\vec{k}}$ such that $q(r_{\vec{k}}) = m/n$. This equation is renormalized by substituting $\tilde{\eta}_{\vec{k}''}$ and $\phi_{\vec{k}''}$ for $\tilde{\eta}^{(2)}_{\vec{k}''}$ and $\phi^{(2)}_{\vec{k}''}$. Here, $\tilde{\eta}^{(2)}_{\vec{k}''}$ and $\phi^{(2)}_{\vec{k}''}$ are driven by the direct beat of the test $(\vec{k})$ and background $(\vec{k}')$ modes. Since the full range of x' is swept over by the $\vec{k}'$ integration, the $\tilde{J}_z = 0$ approximation is not valid for the driven modes $(\vec{k}'')$. Thus, in order to simplify the renormalization procedure, $\phi^{(2)}_{\vec{k}''}$ (associated with shielding effects) is neglected. Thus $\tilde{\eta}^{(2)}_{\vec{k}''}$ is given by

$$\tilde{\eta}^{(2)}_{\vec{k}''} = \left(ik'_\theta \, \phi_{\vec{k}'} \frac{\partial \tilde{\eta}_{\vec{k}}}{\partial x} - \frac{\partial \phi_{\vec{k}'}}{\partial x'} ik_\theta \tilde{\eta}_{\vec{k}} + ik_\theta \phi_{\vec{k}} \frac{\partial \tilde{\eta}_{\vec{k}'}}{\partial x'} \right.$$

$$\left. - ik'_\theta \frac{\partial \phi_{\vec{k}}}{\partial x} \tilde{\eta}_{\vec{k}'} \right) \left[\gamma_{\vec{k}+\vec{k}'} + \chi_\parallel (k_\parallel + k'_\parallel)^2 \right]^{-1}$$

Substituting $\tilde{\eta}^{(2)}_{\vec{k}''}$ into the nonlinear equation, noting that $\tilde{\eta}_{-\vec{k}} = \tilde{\eta}_{\vec{k}}$ and $\phi_{-\vec{k}} = \phi_{\vec{k}}$, and retaining only the dominant radial diffusion term (as the radial wave number exceeds the poloidal wave number) yields the renormalized resistivity equation:

$$\frac{\partial \tilde{\eta}_{\vec{k}}}{\partial t} + \chi_\parallel k_\parallel^2 \tilde{\eta}_{\vec{k}} - D_{\vec{k}} \frac{\partial^2 \tilde{\eta}_{\vec{k}}}{\partial x^2} = -ik_\theta \phi_{\vec{k}} \frac{d\eta_0}{dr} , \tag{11a}$$

$$D_{\vec{k}} = \sum_{\vec{k}''} k''^2_\theta |\phi_{\vec{k}''}|^2 \left[\gamma_{\vec{k}+\vec{k}''} + \chi_\parallel (k_\parallel + k''_\parallel)^2 \right]^{-1} . \tag{11b}$$

Here $D_{\vec{k}}$ accounts for the crucial nonlinear effect, which is random convection of $\tilde{\eta}$ by fluid turbulence. In Eq. (11b), $\vec{k}''$ refers to the background spectrum produced by modes of neighboring helicities.

Noting that when $\tilde{J}_z = 0$, $\phi_{\vec{k}} \sim \tilde{\eta}_{\vec{k}}/x$, it follows that for stationary turbulence $(\partial \tilde{\eta}_{\vec{k}}/\partial t = 0)$, the radial structure of $\tilde{\eta}_{\vec{k}}$ is determined by the asymptotic balance of thermal conduction with diffusion. This yields a radial scale for $\tilde{\eta}_{\vec{k}}$ given by

$$\Delta^c_{\vec{k}} = \left(D_{\vec{k}} / \chi_\parallel k'^2_\parallel \right)^{1/4} ,$$

where $k_\parallel = k'_\parallel x$. As $\Delta^c_{\vec{k}}$ is amplitude dependent (through $D_{\vec{k}}$), it follows that, in the nonlinear regime, the basic radial scales for $\tilde{\eta}$ and ϕ are

determined not by the linear eigenmode width but rather by the turbulent correlation length. This length is in turn determined by the coupling of radial diffusion and radially varying parallel thermal conduction. Thus, it is clear that the saturated state, characterized by $\tilde{J}_z = 0$ and by a nonlinear scale size $\Delta^c_{\vec{k}}$, is radically different in character from the linear regime.

At this point it is useful to indicate the correspondence between $\Delta^c_{\vec{k}}$ and the scale length $x_c = (D/k'_{\parallel} v_{Te})^{1/3}$, defined in Ref. 11. Recall that x_c is the radial correlation length associated with shear-induced resonance broadening; that is, $x_c = \omega_c / k'_{\parallel} v_{Te}$, where $\omega_c = (k'^2_{\parallel} v^2_{Te} D)^{1/3}$ is the electron decorrelation rate for radial diffusion in a sheared magnetic field. In that problem, radial diffusion coupled to radially dependent single-particle ballistic streaming ($\sim k'_{\parallel} v_{Te} x$) to yield a correlation length $x_c \sim D^{1/3}$. Here, radial diffusion couples to radially dependent parallel thermal diffusion ($\sim k'^2_{\parallel} \chi_{\parallel} x^2$) to yield a correlation length $\Delta^c_{\vec{k}} \sim D^{1/4}$. Thus, in both cases the nonlinear decorrelation mechanism involves the coupling of radial diffusion to the shear-induced radial dependence of $k_{\parallel}$.

Another consequence of the condition $\tilde{J}_z = 0$ is that the second saturation criterion $\partial E_T / \partial t = 0$ reduces to

$$\int dx \, \chi_{\parallel} k^2_{\parallel} |\tilde{\eta}_{\vec{k}}|^2 = \int dx \, \frac{L_s}{L_\eta} E_0 \frac{|\tilde{\eta}_{\vec{k}}|^2}{x} , \qquad (12)$$

where $E_0 = \eta_0 J_{z0}$, and it is understood that $x \approx 0$ is excluded from the domain of integration. The prescription for resolving the $x = 0$

singularity is discussed below. The structure of the right-hand side of Eq. (12) illustrates the intimate connection between the rippling instability and the asymmetric (in x) spectrum structure, since for $|\tilde{\eta}_{\vec{k}}|^2$ even in x, the driving term, which contains the free energy source $(1/L_\eta)$, would vanish. Also, the asymmetry of $|\vec{\eta}_{\vec{k}}|^2$ is another indication of the irrelevance of the $x \approx 0$ region to the rippling mode dynamics. Equation (12) is homogeneous (in explicit dependence) in resistivity fluctuation level and is only satisfied when the amplitude dependent radial scale (correlation) length adjusts to the value determined by Eq. (12). Using Eq. (12), it follows that saturation occurs for

$$\Delta^c_{\vec{k}} \approx \left(\frac{L_s E_0}{L_\eta B_z}\right)^{1/3} (\chi_\parallel k_\parallel'^2)^{-1/3} ,$$

which requires that

$$D_{\vec{k}} \approx \left(\frac{L_s E_0}{L_\eta B_z}\right)^{4/3} (\chi_\parallel k_\parallel'^2)^{-1/3} . \qquad (13)$$

Equation (13) states that saturation occurs when turbulent diffusion is large enough so that dissipation due to parallel thermal conduction, proportional to $\chi_\parallel (k_\parallel' \Delta^c_{\vec{k}})^2$, balances the resistivity gradient driving term, proportional to $(L_s/L_\eta)E_0/\Delta^c_{\vec{k}}$. The length $\Delta^c_{\vec{k}}$ can be viewed as an amplitude-dependent mixing length, which adjusts so that source and sink terms balance, thus satisfying the condition $\partial E_T/\partial t = 0$. In this picture, the nonlinear saturation mechanism is radial-diffusion-induced thermal dissipation, which occurs through the coupling of radial

diffusion to radially varying parallel thermal conduction. Physically, damping occurs when a resistivity fluctuation parcel is first scattered to finite x (and hence finite $k_{\parallel}$) by diffusion and then destroyed by thermal dissipation, proportional to $\chi_{\parallel}(k_{\parallel}'\Delta_{\vec{k}}^{c})^2$. Alternatively, it may be said that because radial diffusion smears out the structure near $x \approx 0$, $\chi_{\parallel}k_{\parallel}'^2x^2$ is always greater than $\chi_{\parallel}(k_{\parallel}'\Delta_{\vec{k}}^{c})^2$, its value with $x = \Delta_{\vec{k}}^{c}$, the radial correlation length.

A quantitative calculation of the level of turbulent diffusion required for saturation is now presented. Using Eqs. (4) and (5), with $\tilde{J}_z = 0$ to eliminate ϕ from Eq. (11), at saturation yields

$$\chi_{\parallel}k_{\parallel}'^2x^2\tilde{\eta}_{\vec{k}} - D_{\vec{k}}\frac{\partial^2\tilde{\eta}_{\vec{k}}}{\partial x^2} = \frac{L_s}{L_\eta}\frac{E_0}{B_z}\frac{1}{x}\tilde{\eta}_{\vec{k}} \ . \tag{14}$$

By a convenient change of variable $x = \Delta_k^c A^{1/3}y$, where $A = L_sE_0\Delta_{\vec{k}}^{c}/(L_\eta D_{\vec{k}})$, Eq. (14) can be written as

$$\frac{\partial^2\tilde{\eta}_{\vec{k}}}{\partial y^2} + A^{4/3}\left(\frac{1}{y} - y^2\right)\tilde{\eta}_{\vec{k}} = 0 \ . \tag{15}$$

Using the WKB phase integral quantization condition, the eigenvalues of Eq. (15) are given by

$$A^{2/3}\lim_{\delta\to 0}\oint\left[\frac{z(1-z^3)}{z^2+\delta^2}\right]^{1/2}dz = p\pi \ . \tag{16}$$

Since $A \sim 1/D_{\vec{k}}$, $p = 1$ corresponds to the largest level of diffusion, so that

$$D_{\vec{k}} = \left[\frac{\Gamma(1/6)\Gamma(1/2)}{2\pi\Gamma(2/3)}\right]^2 \left(\frac{L_s E_0}{L_\eta B_z}\right)^{4/3} (\chi_{\parallel} k_{\parallel}'^2)^{-1/3} \qquad (17)$$

at saturation. Apart from the numerical factor, the results of Eqs. (13) and (17) are identical.

A striking characteristic of the level of saturation for the kinetic energy predicted by Eq. (17) is the comparatively weak dependence on $\chi_{\parallel}$. This is in marked contrast to any expectation based on the linear theory, in which the linear growth rate scales as $\chi_{\parallel}^{-4/3}$. Furthermore, it is in disagreement with a previous result obtained by these authors and reported in Ref. 6. In that paper, the level of diffusion at saturation was estimated by balancing $\chi_{\parallel}(k_{\parallel}'\Delta_{\vec{k}}^c)^2$ with the linear growth rate γ, yielding $D_{\vec{k}}$. Thus, while the nonlinear damping mechanism was the same, the driving term in the saturated state was erroneously approximated by the linear growth rate. Here, the $\tilde{J}_z = 0$ condition has facilitated a more accurate approximation of the nonlinearly relevant driving term as $(L_s E_0/L_\eta)/\Delta_{\vec{k}}^c$, which results in a weaker scaling of $D_{\vec{k}}$ with $\chi_{\parallel}$. In retrospect, the previous result yielded, in essence, a measure of the level of diffusion at which the system undergoes the transition from linear $[\gamma > D_{\vec{k}}/(\Delta_{\vec{k}}^c)^2]$ to nonlinear $[\gamma < D_{\vec{k}}/(\Delta_{\vec{k}}^c)^2]$ regimes, rather than the actual saturation level itself. It is readily apparent that the level of diffusion at saturation is significantly larger than that for which $\chi_{\parallel}(k_{\parallel}'\Delta_{\vec{k}}^c)^2 \sim \gamma$. Thus, this

problem is an example of a nonlinear theory that addresses the mechanisms of both saturation and drive in the stationary state. Also, it is instructive to remark that the large difference between the levels of diffusion at transition and saturation is an indication of the errors that may result from the use of oversimplified mixing length "rules," such as $D \sim \gamma/k_\perp^2$. Finally, it should also be noted that, as in the case studied in Ref. 6, the mechanism of diffusion-induced thermal dissipation, rather than quasi-linear flattening of the resistivity gradient, is the dominant saturation mechanism.

The validity and limitations of the assumption $\tilde{J}_z = 0$ have been studied by numerically solving the renormalized equations for the resistivity evolution, Eq. (11), together with the ϕ evolution equation in the steady-state limit. They are:

$$D_{\vec{k}} \frac{\partial^2 \tilde{\eta}_{\vec{k}}}{\partial x^2} - \chi_{\parallel} k_{\parallel}'^2 x^2 \tilde{\eta}_{\vec{k}} + i k_\theta \eta_0 \frac{1}{L_\eta} \phi_{\vec{k}} = 0 \ , \tag{18}$$

$$\mu \frac{\partial^4 \phi_{\vec{k}}}{\partial x^4} - \frac{1}{\eta_0} k_{\parallel}'^2 x^2 \phi_{\vec{k}} - i \frac{J_{z0}}{B_z \eta_0} k_{\parallel}' x \tilde{\eta}_{\vec{k}} = 0 \ . \tag{19}$$

Equations (18) and (19) reduce to Eq. (14) in the limit $\mu = 0$, which is equivalent to the $\tilde{J}_z = 0$ condition. This system of equations has been solved as an eigenvalue problem. Here $D_{\vec{k}}$ is taken to be the eigenvalue for a given viscosity μ. An anomalous viscosity μ is generated by fluid convection and can easily be estimated by following the procedure used to obtain $D_{\vec{k}}$. However, since the convective nonlinearity of

Eq. (5) conserves energy, replacing the nonlinearity by a simple viscosity is not, in general, an adequate renormalization procedure. Indeed, a simple $\mu\,\partial^2/\partial x^2$ is an overestimate of dissipation. However, the basic features of the result, that sensitivity of $D_{\vec{k}}$ to $\chi_{\parallel}$ increases, do not change when a more sophisticated renormalization is used. In Fig. 1 the calculated values of $D_{\vec{k}}$ are compared with the analytic result, Eq. (17), obtained in the limit $\mu = 0$. The calculations have been done for equilibrium parameters close to characteristic plasma edge parameters in the Macrotor[1] tokamak: namely, $L_\eta = 0.3a$, $L_s = 4.2a$, $r_s = 0.75a$, $S = 10^5$, and $10^4 < \bar{\chi}_{\parallel} < 10^7$, where $\bar{\chi}_{\parallel} = \chi_{\parallel}\tau_R/R_0^2$. For $\mu = 0$ the analytic results agree well with the numerical ones. There is a reduction of the level of diffusion required for saturation as viscosity increases. This effect is stronger at high $\chi_{\parallel}$, and it increases the dependence of $D_{\vec{k}}$ on $\chi_{\parallel}$ for finite $\tilde{J}_z$.

To conclude this section, it is worthwhile to add that the nonlinear theory developed here is essentially one of a renormalized resistivity response calculation. This analysis yields insight into the nonlinear space and time scales $\Delta^c_{\vec{k}}$ and $(\chi_{\parallel}(k'_{\parallel}\Delta^c_{\vec{k}})^2)^{-1}$, analogous to the eddy size and eddy turnover time of fluid turbulence, respectively, that are necessary for construction of a basic nonlinear theory and calculation of fluctuation levels. However, detailed calculation of fluctuation spectra requires construction of a two-point theory for $\langle\tilde{\eta}(r_1)\tilde{\eta}(r_2)\rangle_{\vec{k}}$, which accounts for incoherent mode coupling as well as the nonlinear coherent response and resistivity gradient drive. The spectrum is then determined by the balance of the difference of

incoherent emission and coherent damping (diffusion) with resistivity gradient drive. The importance of incoherent mode coupling is easily seen by noting that the nonlinearity $\vec{\nabla}\phi \times \hat{z} \cdot \vec{\nabla}\eta$ conserves E_T but the renormalized coherent response equation [Eq. (11)] does not. However, none of the results of this paper are sensitive to this deficiency, which will be rectified in a future publication. Finally, in lieu of an analytical calculation of the poloidal mode number spectra, numerical results are used to compute $(m)_{rms}$ when necessary.

IV. MULTIPLE-HELICITY RIPPLING MODE CALCULATIONS

Numerical studies of multiple-helicity rippling mode turbulence have been done using the basic rippling mode model described in Sec. III. The nonlinear equations, Eqs. (1)-(3), are solved by a nonlinear three-dimensional (3-D) initial value code KITE.[8] The numerical method used in this code is finite differences in the radial variable r and spectral representation in the poloidal angle θ and toroidal angle $\zeta = z/R_0$. The time integration is first order accurate, and all of the linear terms are treated implicitly. For details on the numerical scheme and convergence studies, see Ref. 8.

When Eqs. (1)-(3) are written in dimensionless form, they depend on two dimensionless parameters S and $\bar{\chi}_{\parallel}$, which are defined in Sec. III. For many of the numerical studies, a viscosity term has been included in Eq. (2). It has the form $R_V^{-1}\nabla_\perp^2 U$. There is also a small perpendicular heat diffusivity term included in Eq. (3), $\bar{\chi}_\perp \nabla_\perp^2 \tilde{\eta}$.

It has been assumed in the numerical calculations that the rippling mode turbulence is localized in the annular region in minor radius. This allows us to treat the problem with a moderate number of modes.

The equilibrium considered here is similar to the characteristic edge plasma conditions in the Macrotor[1] tokamak. An electron temperature profile

$$T_{e0}(r) = T_{e0}(0)\left[1 + (r/r_0)^2\right]^{-4/3}$$

is asumed for the numerical calculations. The resistivity profile is then determined by the Spitzer relation. The equilibrium current profile, J_{z0}, is chosen to be consistent with a resistive equilibrium. The safety factor q profile is determined by taking $q(0) = 1$. The value of r_0 is then fixed by setting the safety factor at the plasma edge $q(a) = 3.5$. This gives $r_0 = 0.632a$. An equilibrium mass density profile

$$\rho_m(r) = \rho_m(0)\left[0.75(1 - r^2/a^2)^2 + 0.25\right]$$

is assumed. This gives a value for $\rho_m = 0.39\rho_m(0)$ in the region of the rippling mode activity. The dimensionless parameters $S = 10^5$ at the magnetic axis and $\bar{\chi}_{\parallel} = 2.5 \times 10^5$ correspond to a peak electron density of 10^{13} cm^{-3}, a toroidal field of 2 kG, and an electron temperature of 15 eV at $r = 0.77a$, the center of the region where the rippling mode turbulence is supposed to be localized. In this region, $S = 10^4$. The major and minor radius for the calculation are taken to be those of

Macrotor, that is, $R_0 = 90$ cm and $a = 45$ cm. The perpendicular diffusion coefficient is fixed for all the calculations to $\bar{\chi}_\perp = 10^{-2}$, and the viscosity term is neglected unless otherwise stated.

Since the equilibrium is an exact, steady-state solution of Eqs. (1)-(3), it is necessary to add a small perturbation to break the symmetry, in order to perform a stability calculation. An initial perturbation is usually added to each Fourier component of the variable ϕ, which has the form

$$\phi_{mn} = W_I\left(\frac{r}{r_s}\right)^m \exp\left[-\frac{(r - \bar{r}_s)^2}{\Gamma}\right] \qquad r \le r_s ,$$

$$W_I\left(\frac{1 - r}{1 - r_s}\right) \exp\left[-\frac{(r - \bar{r}_s)^2}{\Gamma}\right] , \qquad r \ge r_s ,$$

where $\bar{r}_s = r_s + \Gamma$, with $\Gamma = 0.0144$. For the calculations described in this paper the normalization constant W_I is taken to be 10^{-5}. All the modes used in the calculation were initialized at this level. The low initial amplitude of the modes allows a separation of the linear phase of the evolution, which is a useful way of controlling the numerics.

To compare the role of quasi-linear stabilization with that of the turbulent stabilization of the rippling modes, the numerical calculations have been performed in two different ways. One way was to allow the free evolution of the resistivity profile. Another alternative was to hold the average resistivity profile constant. The latter can be justified by the balance of the ohmic heating and thermal diffusion in an actual tokamak and is probably a more realistic way of simulating the experiment. Comparisons between these two types of evolution are given in this section.

Let us first discuss the effect of turbulent stabilization of rippling modes. For this purpose, the numerical calculations must be done with a relatively large value of $\chi_{\parallel}$, in order to detect its effects with a moderate number of modes in the calculation. If $\chi_{\parallel}$ is too large, the unstable spectrum of rippling modes is too narrow and the assumptions used in the theory of turbulent saturation are no longer valid. The dependence of the linear growth rate on $\bar{\chi}_{\parallel}$, discussed in Sec. II, can be used to make an estimate of the relevant number of modes m to be considered in the calculation,

$$m \leq 10 \left(\frac{S}{\bar{\chi}_{\parallel}}\right)^{5/4} S^{1/4} .$$

For Macrotor parameters, $m < 50$. This indicates that for these values of the parameters a full 3-D calculation is feasible. Several nonlinear calculations have been done for different numbers of modes, namely, 2, 13, 49, 108, and 177 modes. The average resistivity profile

has been held constant for all these calculations. In Fig. 2 the mean-square radial velocity

$$\bar{E} = \sum_{m,n} \left| \frac{m}{r} \phi_{mn} \right|^2$$

is plotted as a function of time for the five different cases. It is clear that, in spite of not allowing the gradient $d\eta_0/dr$ to relax, there is a strong stabilization effect associated with increasing the number of modes. It is also apparent that $\bar{E}$ saturates when a sufficient number of modes is included in the calculation.

When only two modes are included, the $(m = 0; n = 0)$ and $(m = 5; n = 2)$, and the $(m = 0; n = 0)$ is held constant in time, the $(m = 5; n = 2)$ grows without limit at its linear growth rate, and there is no saturation. Including 13 modes, the nonlinear stabilization effects are obvious; nevertheless, they are not sufficient to reach a saturated state. It is necessary to include 49 or more modes to reach saturation. Reasonably converged results are obtained with about 100 modes. It is important to look at the effect of the nonlinear stabilization on individual modes. Figure 3 shows the kinetic energy for the $(m = 5; n = 2)$ and $(m = 28; n = 12)$ modes for the different cases being considered. For the calculation with 13 modes the $(m = 28; n = 12)$ mode is not included. It is clear that, for a given test mode, the convergence of the results depends on the number of modes to which it is nonlinearly coupled. For a fixed set of modes, because of the method of mode selection, the $m = 5$ mode couples to more modes than the $m = 28$. Namely, for the case with 49 modes the $m = 5$

couples to 45 modes; the m = 28, only to 23. Hence, convergence of the kinetic energy of the m = 5 mode is achieved with a lower number of modes. The m = 5 mode is slightly stabilized for the 13-mode case but, since the number of modes is insufficient, the mode does not saturate. Although the m = 28 saturates for the case with 49 modes, the level of saturation is five times larger than the converged value. The amplitude of the oscillations around the saturated level decreases with increasing number of modes. The frequency of oscillations is very high. To clarify the comparisons of results with different numbers of modes, the plotted results have been averaged over this fast frequency. This high-frequency oscillation is discussed later in this section.

As previously mentioned, the number of modes required to observe the turbulent stabilization at low values of $\bar{\chi}_{\|}$ can be very high. Nonlinear calculations have been done for the same Macrotor-type equilibrium, changing only the value of $\bar{\chi}_{\|}$ from $\bar{\chi}_{\|} = 2.5 \times 10^5$ to $\bar{\chi}_{\|} = 10^4$. Nonlinear stabilization effects were also clearly observed for this case. However, it was not possible to obtain converged results with a number of modes and grid points that can be handled reasonably.

All the numerical results show very clear evidence of a nonlinear saturation mechanism, totally unrelated to the quasi-linear flattening of the resistivity gradient. It is interesting to compare the situation in which both stabilization mechanisms can compete with each other. This can be done by letting the resistivity profile relax during the nonlinear evolution. A calculation has been done for the same equilibrium parameters as before, including 108 modes. In Fig. 4

the evolution of $\bar{E}$ for the two cases is compared. Figure 5 shows the evolution of the kinetic energy for the (m = 5; n = 2) and (m = 28; n = 12) modes for both types of nonlinear evolution. The level of saturation with quasilinear flattening allowed is lower than that for the case in which the resistivity profile is held constant. This different level of saturation is due primarily to the m = 5 mode (Fig. 5a), the lowest m mode included in the calculation. The level of saturation of the high-m modes is almost unchanged (Fig. 5b). However, the frequency of oscillations around the saturated value is clearly different. Here, the high frequency oscillations of the kinetic energy of the individual modes have been retained. In the case of the frozen resistivity profile, the oscillations are high frequency, with period $\tau \approx \left[\chi_{\parallel}(k_{\parallel}'\Delta_{\vec{k}}^{c})^2_{rms}\right]^{-1}$. In the case where η_0 is not frozen, the oscillations are low frequency, on the time scale of the fluctuations in $d\eta_0/dr$ caused by convection of η_0 by the (m = 5; n = 2) mode.

The numerical calculation can also be used to directly test the condition $\tilde{J}_z = 0$, which has been used in the analytic theory of resistivity-gradient-driven turbulence. For the (m = 5; n = 2) mode at saturation, the functions $\nabla_{\parallel}\phi$, $\eta_0\tilde{J}_z$, and $\tilde{\eta}J_{z0}$ have been plotted. In Fig. 6 it can be seen that in the relevant region, near the peak of ϕ, the condition $\tilde{J}_z = 0$ is approximately verified.

From Eq. (13) it is clear that the level of turbulent diffusion required to saturate an (m;n) rippling mode scales as $m^{-2/3}$. Therefore, in the numerical calculation, the nonlinear stabilization effects are evident first for high-m modes and, as the level of turbulence increases, are then manifested in low-m modes. It is interesting to make a more quantitative estimate of this effect. To do so, ignoring the $k_{\parallel}$ dependence of $D_{\vec{k}}$, one can express the level of resistivity diffusion in terms of the mean-square radial velocity

$$D_{\eta}(t) = \left[\frac{\bar{E}(t)}{\chi_{\parallel}^{1/2}(k_{\parallel}')_{rms}}\right]^{2/3} ,$$

where it is explicitly shown that the mean-square radial velocity is a function of time in the calculation (Fig. 2). The time at which a test mode $\vec{k} = (m; n)$ saturates is given by the equation

$$D_{\vec{k}} = D_{\eta}(t) .$$

Then, using Eq. (17), it is possible to calculate the mean-square radial velocity required to stabilize the test mode,

$$\bar{E} = 1.55 \frac{(m)_{rms}}{m} \left(\frac{L_s E_0}{L_{\eta} B_z}\right)^2 .$$

In Fig. 7 the value of $\bar{E}$ has been plotted vs m for the particular parameters of the numerical calculation. The value of $\bar{E}$ for which the

different modes present in the calculation are stabilized is also plotted in the same figure, in the form of a histogram. The modes have been divided into five groups, in relation to their m value, and the level of mean-square radial velocity required for stabilization is defined as the value of $\bar{E}$ when the net nonlinear growth rate of the mode becomes zero. There is a clear correlation between the analytically calculated value and the numerical results.

V. FLUCTUATION LEVEL AND TRANSPORT

Having elucidated the basic nonlinear saturation mechanism and calculated $D_{\vec{k}}$ at saturation, it is now possible to estimate a number of relevant quantities that characterize saturated resistivity-gradient-driven turbulence. These include the mean-square radial velocity, and the rms potential, density, and resistivity fluctuation levels. Ignoring the $k_{\parallel}$ dependence of $D_{\vec{k}}$ (which constitutes a Markovian approximation, already tacitly assumed), Eq. (17) can be rewritten as

$$\sum_{\vec{k}''} \frac{E_{\vec{k}''}}{\chi_{\parallel}\left[(k_{\parallel}'')^2 \Delta^c_{\vec{k}''}\right]^2} = 1.34\left(\frac{L_s E_0}{L_\eta B_z}\right)^{4/3} (\chi_{\parallel} k_{\parallel}'^2)^{-1/3} , \tag{20}$$

where $E_{\vec{k}} = k_\theta^2 |\phi_{\vec{k}}|^2$ and, consistent with the fact that summation over $\vec{k}''$ sweeps the background turbulence response function over its radial width $\Delta^c_{\vec{k}''}$, x'' was approximated as $\Delta^c_{\vec{k}''}$. Thus, taking $k_\theta \sim (k_\theta)_{rms}$, it follows that

$$\bar{E} = \sum_{\vec{k}} E_{\vec{k}} \approx 1.55 \left(\frac{L_s E_0}{L_\eta B_z}\right)^2 \tag{21}$$

and

$$(\tilde{V}_r)_{rms} \approx 1.23 \frac{L_s E_0}{L_\eta B_z} , \tag{22}$$

$$\left(\frac{e\phi}{T_e}\right)_{rms} \approx 1.23 \frac{L_s}{L_\eta} \frac{E_0}{B_z} \frac{1}{c_s \rho_s (k_\theta)_{rms}} . \tag{23}$$

Here $\tilde{v}_r$ is the radial fluid velocity, $c_s = (T_e/m_i)$, and $\rho_s = c_s/\Omega_i$, where m_i and Ω_i are the ion mass and gyrofrequency, respectively. Finally, it should be noted that the somewhat puzzling absence of a $\chi_\parallel$ dependence of $\bar{E}$ can be resolved by inclusion of a viscosity μ, as discussed in Sec. III.

In similar fashion, the rms resistivity fluctuation can be estimated as

$$\left(\frac{\tilde{\eta}}{\eta_0}\right)_{rms} \approx 1.23 \frac{1}{\chi_\parallel (k_\parallel'^2)_{rms} (\Delta_{\vec{k}}^c)^2} \frac{L_s E_0}{L_\eta^2 B_z} .$$

It follows that

$$\left(\frac{\tilde{\eta}}{\eta_0}\right)_{rms} \approx 1.06 \frac{1}{L_\eta} \left(\frac{L_s E_0}{L_\eta B_z}\right)^{1/3} \left[\chi_\parallel (k_\parallel'^2)_{rms}\right]^{-1/3} . \tag{24}$$

Note that $(\tilde{\eta}/\eta_0)_{rms} \sim \Delta^c/L_\eta \sim n^{1/3} T_e^{-5/6}$. Thus, the resistivity fluctuations increase rapidly with increasing radius as T_e decreases.

These results can be compared with the mean-square radial velocity and rms potential and resistivity fluctuation levels obtained in the 3-D numerical calculations described in the last section. To do this, it is necessary to have an estimation of $(m)_{rms}$. As the spectrum is peaked at low m, it is tempting to use the lowest m value in the calculation, namely m = 5. However, the correct procedure is to calculate $(m)_{rms}$ at saturation. In Fig. 8 the rms m has been plotted as a function of time. The saturated value is $(m)_{rms} = 6.8$, which indicates the peaking of the spectrum at low m. Using this value, the rms resistivity fluctuation level can be calculated from Eq. (24), and one finds $(\tilde{\eta}/\eta_0)_{rms} = 5.2 \times 10^{-2}$; that is, $(\tilde{T}/T_0) = 3.5 \times 10^{-2}$. The mean-square radial velocity calculated with Eq. (21) is $\bar{E} = 303a^2/\tau_R^2$. These values compare well with the numerical results. In Fig. 9 the time evolution of the mean-square radial velocity, radial magnetic field, temperature, and density is given. From this, the mean-square radial velocity at saturation is found to be $\bar{E} = (375 \pm 25)a^2/\tau_R^2$, and the mean-square temperature fluctuation is $(\tilde{T}/T_0) = 4.9 \times 10^{-2}$. These values agree well with the predictions of the analytic model.

In addition to the quantities estimated above, the rms density fluctuation is of considerable interest in the context of experimental edge turbulence studies. The basic rippling instability model does not include density dynamics, and it is difficult to properly and self-consistently account for density evolution without a significant departure from the very simple model adopted here. Nevertheless, some insight into the level of density fluctuations driven by the rippling mode turbulence can be gained by consideration of a model in which the

density n evolves by convection as a passive scalar in the field of fluid turbulence, determined by Eqs. (4)-(6). In this model, the density perturbation n evolves according to

$$\frac{\partial \tilde{n}}{\partial t} + (\vec{\nabla}_\perp \phi \times \hat{z}) \cdot \vec{\nabla} \tilde{n} = -\tilde{v}_r \frac{dn_0}{dr} . \tag{25}$$

As before, the rms density fluctuation level at resistivity fluctuation saturation can be estimated by

$$\left(\frac{\tilde{n}}{n_0}\right)_{rms} \approx \tau_c^n \left(\frac{L_s E_0}{L_\eta B_z}\right) \frac{1}{L_n} , \tag{26}$$

where $L_n = [d(\ln n_0)/dr]^{-1}$ and τ_c^n is the density response correlation time, which, since $\tilde{n}$ is convected as a passive scalar, is the fluid eddy turnover time. Hence, $\tau_c^n \approx (\tilde{v}_{rms}/\Delta_n)^{-1}$, where Δ_n is the radial scale length of the density perturbation. As it is appropriate to consider the relative size of density and resistivity fluctuations, it is useful to define

$$R = \frac{(\tilde{\eta}/\eta_0)_{rms}}{(\tilde{n}/n_0)_{rms}} .$$

Using Eqs. (22) and (24), it follows that

$$R \approx \frac{\tau_c^\eta}{\tau_c^n} \frac{L_n}{L_\eta} ,$$

where $\tau_c^\eta = [\chi_{||}(k_{||}' \Delta_{\vec{k}}^c)^2]^{-1}$. Since the enhanced decorrelation effects related to parallel thermal conduction do not play a role in density dynamics, $\tau_c^\eta < \tau_c^n$ since $\Delta_n > \Delta_k^c$. Thus, for $L_n \sim L_\eta$, $R < 1$ and $(\tilde{\eta}/\eta_0)_{rms} < (\tilde{n}/n_0)_{rms}$. Using Eqs. (13) and (22) for $\Delta_{\vec{k}}^c$ and $\vec{v}_{rms}$, respectively, it follows that, more generally,

$$R \approx \frac{L_n}{L_\eta} \frac{\Delta_{\vec{k}}^c}{\Delta_n} . \qquad (27)$$

Thus, rippling mode turbulence can support a moderate level of density fluctuation that exceeds the level of resistivity (temperature) fluctuation.

When comparing resistivity and density fluctuation levels determined by numerical solution of the equations, it is important to note that due to the absence of dissipation in the density evolution equation, the energy

$$E_N = \frac{1}{2} \int d^3x \ |\tilde{n}|^2$$

evolves according to

$$\frac{\partial E_N}{\partial t} = -\int d^3x \ (\tilde{n}^* \tilde{v}_r) \frac{dn_0}{dr}$$

and thus grows without saturation when dn_0/dr is held constant. Of course, in reality density evolution is controlled by dissipation associated with coupling to outgoing ion sound waves and thus, ultimately, ion Landau damping. However, examination of R at the time of resistivity fluctuation saturation can provide some insight into the relative magnitude of the density and resistivity fluctuations. This has been done using the numerical calculations. Equation (25) is solved together with Eqs. (1)-(3), not as part of the dynamical model, but as a diagnostic for the induced density fluctuations. Note that the density calculated with Eq. (25) does not couple back to Eqs. (1)-(3). In Fig. 10 the time evolution of R is plotted. At the saturation of the resistivity fluctuations, R = 0.3. For the particular resistivity and density profiles used in the calculation, $L_\eta/L_n = 1.5$, the resistivity width $\Delta_{\vec{k}}^c \cong 0.06a$, and the density width $\Delta_n \cong 0.14a$. Therefore, the value of R is consistent with Eq. (27). The density fluctuation level at saturation is $(\tilde{n}/n_0) = 0.22$, using the Macrotor parameters and the value of $(\tilde{\eta}/\eta_0)$ obtained in the numerical calculation.

Thus, in contrast to a statement made in Ref. 12, resistivity-gradient-driven turbulence, which evolves from rippling modes, can produce large density fluctuations. Also, since significant deviation from adiabatic density response $(\tilde{n}/n_0 \sim e\phi/T_e)$ has been observed experimentally,[13] the viability of this model does not depend on its predicted relationship between density and potential fluctuations.

In order to complete our study of rippling mode turbulence, the thermal and particle transport in the saturated state is now discussed. Since η_0 evolves by electrostatic convection (conduction being negligible for relevant $\chi_{\parallel}$ and $\tilde{\psi}$ levels), it follows that the resistivity (temperature) flux Γ_η is

$$\Gamma_\eta = \sum_{\vec{k}} (\tilde{V}_r^*)_{\vec{k}} \frac{\tilde{\eta}_{\vec{k}}}{\eta_0} . \tag{28}$$

Using the rms values of $\tilde{v}_r$ and $(\tilde{\eta}/\eta_0)$ given in Eqs. (22) and (24), respectively, to estimate Γ_η, it is easily verified that

$$\Gamma_\eta = 1.34 \left(\frac{L_s E_0}{L_\eta B_z}\right)^{4/3} \left(\chi_{\parallel} \langle k_{\parallel}'^2 \rangle_{rms}\right)^{-1/3} \frac{1}{L_\eta} , \tag{29}$$

and the resistivity (thermal) diffusivity D_η is given by

$$D_\eta \approx 1.34 \left(\frac{L_s E_0}{L_\eta B_z}\right)^{4/3} \left(\chi_{\parallel} \langle k_{\parallel}'^2 \rangle_{rms}\right)^{-1/3} .$$

Note that D_η is the same as $D_{\vec{k}}$ with $k_{\parallel}'^2$ evaluated at the rms value. In particular, the dependence of D_η on $\chi_{\parallel}$ is quite weak. For Macrotor plasma edge parameters, $D_\eta = 8.6 \times 10^3 \, cm^2/sec$.

Similarly, the density flux Γ_η is given by

$$\Gamma_n = \sum_{\vec{k}} (\tilde{v}_r^*)_{\vec{k}} \frac{\tilde{n}_{\vec{k}}}{n_0} . \tag{30}$$

Thus, evaluating Γ_n by a procedure similar to that used in the evaluation of Γ_η, it follows that $\Gamma_n = \Gamma_\eta/R$, and

$$D_n = \frac{1}{R} \frac{L_n}{L_\eta} D_\eta , \tag{31}$$

where D_n and D_η are the density and resistivity diffusivities, respectively. Since $R < 1$, it is apparent that rippling mode turbulence can support moderate levels of density transport at smaller levels of thermal transport. For Macrotor parameters, Eq. (31) predicts a density diffusion coefficient $D_n = 1.7 \times 10^4 cm^2/sec$.

VI. SUMMARY AND CONCLUSIONS

An analytic theory of nonlinear evolution and saturation of resistivity-gradient-driven turbulence has been developed. The nonlinear saturation mechanism has been identified. The saturation mechanism is the turbulent diffusion of the resistivity fluctuation into the region of large damping due to parallel heat conduction. The basic model of the resistivity-gradient-driven turbulence and the saturation mechanism have been confirmed by detailed numerical calculations. The main results of the theory are as follows:

(i) The vorticity equation decouples from the resistivity evolution and Ohm's law, $\tilde{J}_z = 0$.

(ii) The dominant nonlinearity is the nonlinear convection of the resistivity. The turbulent radial diffusion, induced by this nonlinearity, coupled to the radial dependent parallel heat conduction is the dominant dynamical effect controlling the nonlinear evolution of the rippling modes.

(iii) The resistivity and potential eigenfunctions have an intrinsically nonlinear character. The eigenfunctions are characterized by an amplitude dependent scale length $\Delta_{\vec{k}}^{c}$.

(iv) At saturation, $\Delta_{\vec{k}}^{c}$ adjusts to a value at which thermal dissipation balances the resistivity gradient drive.

(v) The turbulent saturation mechanism is the dominant mechanism when the average resistivity gradient is maintained by an adequate balance with ohmic heating.

Having studied in a sequence of papers the quasi-linear saturation,[5] the transition to nonlinear evolution,[6] and in this paper the nonlinear saturation of these resistive MHD instabilities, we now briefly indicate their differences and interrelationships. This is done in terms of the radial decorrelation length δx and the decorrelation time δt. The values obtained in the various levels of nonlinear models (at least from a scaling standpoint) for these quantities and thus for the maximum radial convection velocity $\tilde{v}_r$ and the resistivity (temperature) diffusion coefficient $D_\eta \sim (\delta x)^2/t$ are indicated in Table I.

There are two important facts to learn from this table. First, the transport characteristics at the turbulent saturation are very different from the commonly used $D \sim \gamma/k_x^2$ quasi-linear time estimate. Although the fundamental drive mechanism (the resistivity gradient) is the same, both the radial the decorrelation length and the decorrelation time are increased and unrelated to their quasi-linear values. Thus, even though the linear growth rate of these modes decreases as $\chi_{\|}^{-4/3}$ for large heat conduction $\chi_{\|}$, $\Delta_{\vec{k}}^{c}$ decreases only as $\chi_{\|}^{-1/3}$, so the effect of these modes in their turbulent state is much larger than might be expected from linear or quasi-linear type estimates.

Second, and equally important, is the fact that the turbulent decorrelation distance or mixing length $\Delta^c_{\vec{k}}$ and the concomitant decorrelation time $\tau^c_{\vec{k}}$ must be determined from a turbulently self-consistent model. Namely, $\Delta^c_{\vec{k}}$ attains the value required for the free energy drive (resistivity gradient) to balance the thermal dissipation (through parallel heat conduction in a sheared magnetic field with turbulent radial diffusion), as discussed in Sec. III.

Thus, we find that in order to properly assess the possible impact of any particular plasma instability, fully turbulent self-consistent models of the free energy sources and the dissipative mechanisms must be developed and solved to determine the relevant "mixing" lengths and times and the consequent transport. Linear/quasi-linear estimates are inadequate and, at least for the rippling mode turbulence we have considered, very misleading in their scaling.

The theory of resistivity-gradient-driven turbulence makes concrete predictions for the saturated level of resistivity (temperature) and potential fluctuations and also allows us to estimate the level of density fluctuations. These predictions, $(\tilde{T}/T_0) \approx 0.05$ and $(\tilde{n}/n_0) \approx 0.25$, are consistent with measured values at the tokamak plasma edge. The main properties of the resistivity-gradient-driven turbulence — fluctuation levels, correlation lengths,[6] and predicted anomalous diffusion coefficients — assert the viability of this model as an explanation of the edge turbulence in tokamaks.

TABLE I. Characteristic decorrelation lengths (δx) and times (δt) and the consequent maximum radial convection velocity $\tilde{v}_r$ and resultant transport (D_η) for various levels of nonlinear models.

	Quasilinear saturation[5]	Transition to nonlinear evolution[6]	Nonlinear saturation (this paper)
δx	x_R (resistive layer width) or Δr_{QL} (heat conduction limited)	Δ_0 (lowest mode decorrelation distance)	$\Delta^c_{\vec{k}}$ (amplitude-dependent mixing length)
δt	γ^{-1}_{linear}	γ^{-1}_{linear}	$\tau^c_{\vec{k}} (\equiv \Delta^c_{\vec{k}}/\tilde{v}_r)$
$\tilde{v}_x$	$\gamma_L x_R \sim \frac{L_s}{L_\eta}\frac{E_0}{B_z} = \frac{\eta}{\mu_0 L_\eta}$	$\gamma_L \Delta_0$	$\frac{L_s}{L_\eta}\frac{E_0}{B_z} = \frac{\eta}{\mu_0 L_\eta}$
D_η	$\gamma_L x_R^2$	$\gamma_L \Delta_0^2$	$(\Delta^c_{\vec{k}})^2/\tau^c_{\vec{k}}$

ACKNOWLEDGMENTS

The authors would like to acknowledge many useful discussions with S. J. Levinson, C. M. Surko, and S. J. Zweben.

This research was sponsored by the Office of Fusion Energy, U.S. Department of Energy, under Contract No. DE-AC05-84OR21400 with Martin Marietta Energy Systems, Inc.

REFERENCES

[1]S. J. Zweben, C. R. Menyuk, R. J. Taylor, Phys. Rev. Lett. 42, 1270 (1979); S. J. Zweben and R. J. Taylor, Nucl. Fusion 21, 193 (1981).

[2]R. E. Slusher and C. M. Surko, Phys. Rev. Lett. 40, 400 (1978).

[3]F. Wagner et al., in Plasma Physics and Controlled Nuclear Fusion Research 1982 (Proc. 9th Int. Conf., Baltimore, 1982) (IAEA, Vienna, 1983), Vol. I, p. 43.

[4]H. P. Furth, J. Killeen, and M. N. Rosenbluth, Phys. Fluids 6, 459 (1963).

[5]B. A. Carreras, J. D. Callen, P. W. Gaffney, and H. R. Hicks, Phys. Fluids 25, 1231 (1982).

[6]J. D. Callen, B. A. Carreras, P. H. Diamond, M. E. Benchikh-Lehocine, L. Garcia, and H. R. Hicks, in Plasma Physics and Controlled Nuclear Fusion Research 1982 (Proc. 9th Int. Conf., Baltimore, 1982) (IAEA, Vienna, 1983), Vol. I, p. 297.

[7]H. R. Strauss, Phys. Fluids 19, 134 (1976).

[8]L. Garcia, B. A. Carreras, J. A. Holmes, and H. R. Hicks, "3-D nonlinear MHD calculations with drift and thermal effects," to be published.

[9]P. H. Rutherford, in Physics of Plasmas Close to Thermonuclear Conditions, edited by B. Coppi (Pergamon Press, Oxford, 1981), p. 143.

[10]P. H. Diamond, R. D. Hazeltine, Z. G. An, B. A. Carreras, and H. R. Hicks, Phys. Fluids 27, 1449 (1984).

[11]S. P. Hirshman and K. Molvig, Phys. Rev. Lett. 42, 648 (1979).

[12]M. Wakatani and A. Hasegawa, Phys. Fluids 27, 611 (1984).

[13]S. J. Levinson, J. M. Beall, E. J. Powers, and R. D. Bengtson, Nucl. Fusion 24, 527 (1984).

FIGURE CAPTIONS

FIG. 1. Diffusion coefficient at saturation as a function of the parallel electron heat conductivity for different values of the anomalous viscosity.

FIG. 2. Mean-square radial velocity as a function of time for calculations with 2, 13, 49, 108, and 177 modes.

FIG. 3. Kinetic energy for the $(m = 5; n = 2)$ and $(m = 28; n = 12)$ modes for the cases in Fig. 2. The $(m = 28; n = 12)$ mode is not included for the calculations with 2 and 13 modes.

FIG. 4. Mean-square radial velocity for calculations with 108 modes when the average resistivity profile is frozen in time and when it is allowed to relax during the evolution.

FIG. 5. Kinetic energy for the $(m = 5; n = 2)$ and $(m = 28; n = 12)$ modes for the cases in Fig. 4.

FIG. 6. The functions ϕ, $\nabla_{\parallel}\phi$, $\eta_0\tilde{J}$ and $\tilde{\eta}J_0$ are shown for the $(m = 5; n = 2)$ mode at saturation in the region near the peak of ϕ. Arbitrary units are used.

FIG. 7. Mean-square radial velocity required to stabilize a given mode vs m. The actual values for which the modes are stabilized in the simulation with 108 modes are also plotted, in the form of a histogram.

FIG. 8. Time evolution of the mean-square m for the case when 108 modes are included in the calculation.

FIG. 9. Time evolution of the mean-square radial velocity, mean-square radial magnetic field, mean-square temperature perturbation, and mean-square density perturbation for the case in Fig. 8.

FIG. 10. Time evolution of R, the ratio of the relative size of density and resistivity fluctuations, for the case in Fig. 8.

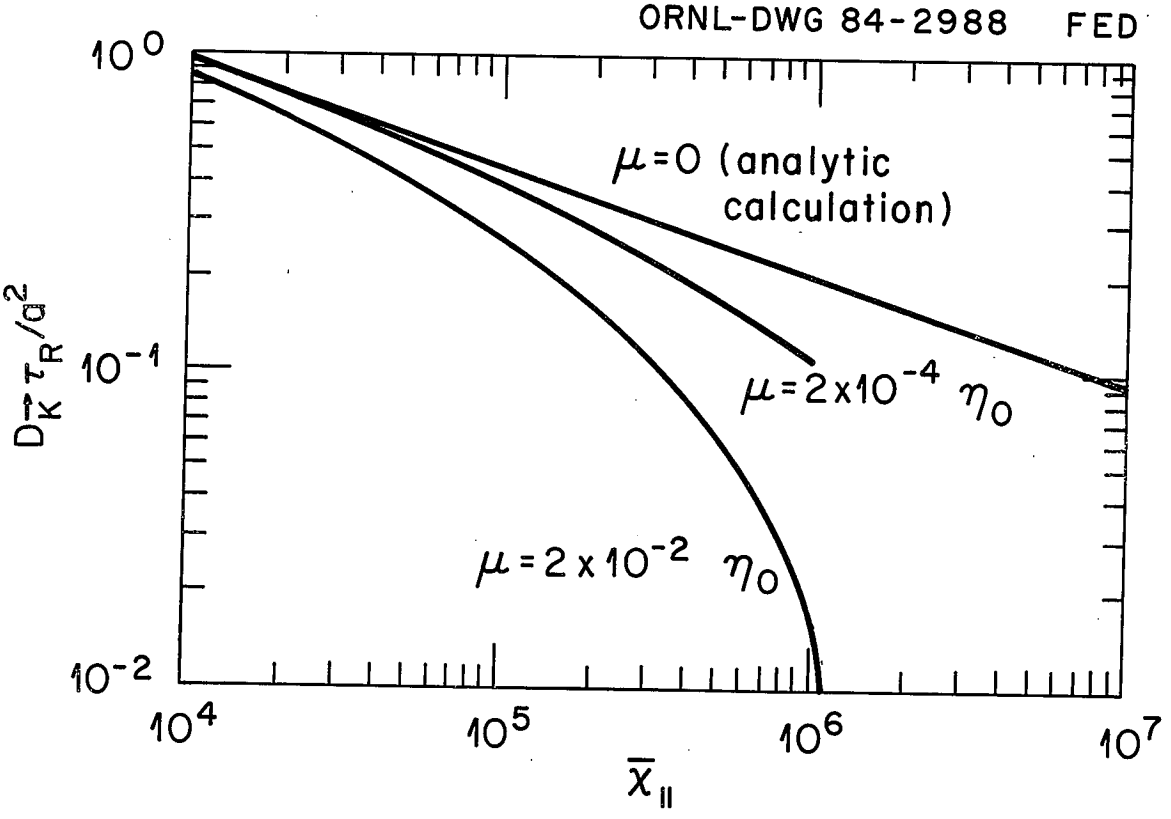
ORNL-DWG 84-2988 FED
10^0
10^{-1}
10^{-2}
$D_K^{\rightarrow} \tau_R / a^2$
$\mu = 0$ (analytic calculation)
$\mu = 2 \times 10^{-4}\ \eta_0$
$\mu = 2 \times 10^{-2}\ \eta_0$
10^4
10^5
10^6
10^7
$\overline{\chi}_{\parallel}$

Fig. 1

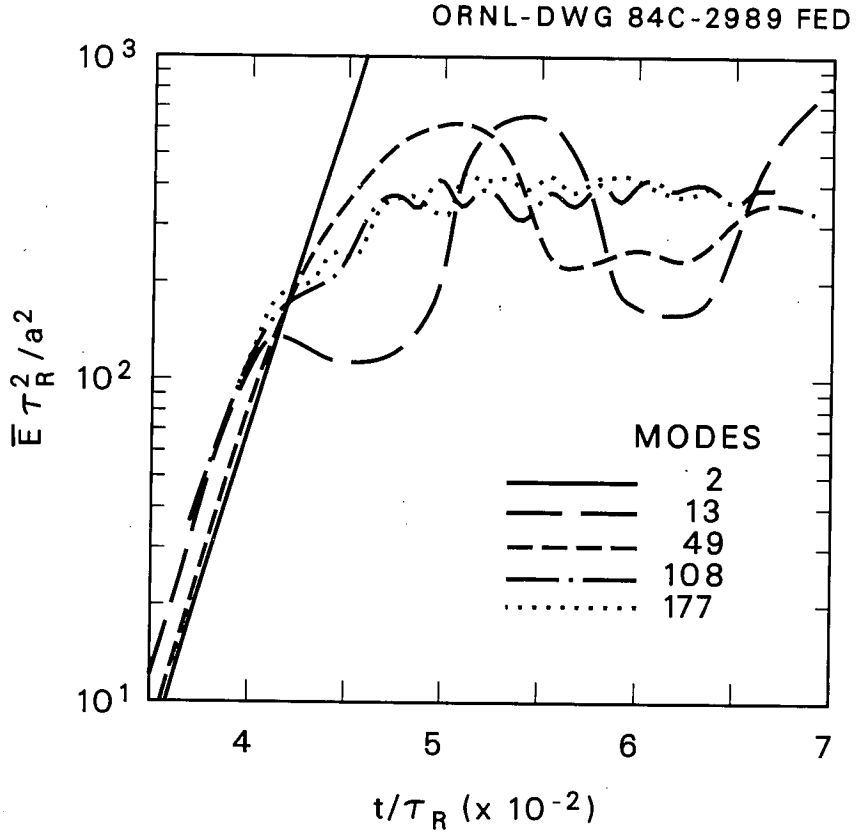
ORNL-DWG 84C-2989 FED
10^3
10^2
10^1
$\bar{E}\tau_R^2/a^2$
MODES
2
13
49
108
177
4
5
6
7
t/τ_R (x 10^{-2})

Fig. 2

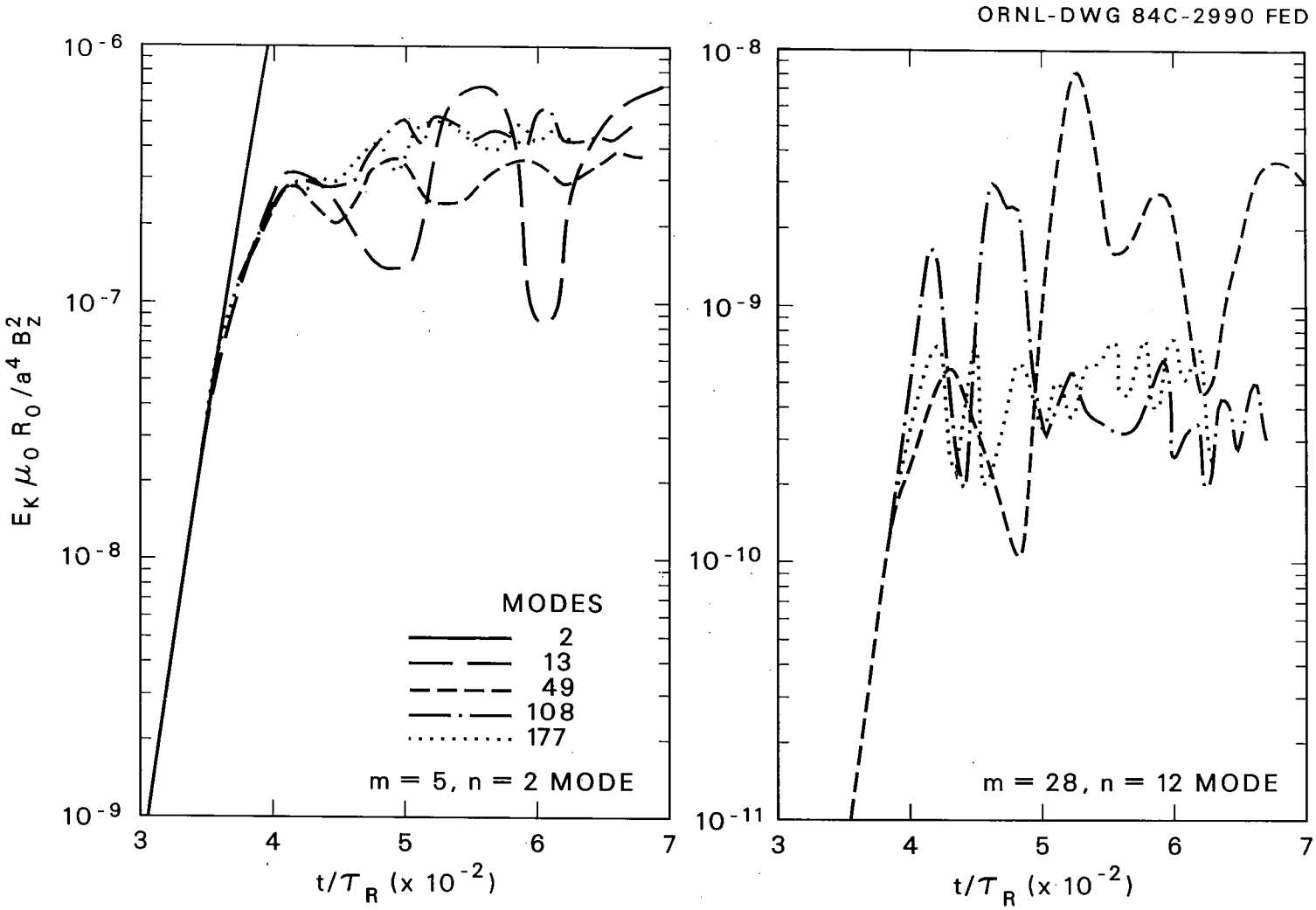
ORNL-DWG 84C-2990 FED
$E_K \mu_0 R_0 / a^4 B_z^2$
10^{-6}
10^{-7}
10^{-8}
10^{-9}
MODES
2
13
49
108
177
m = 5, n = 2 MODE
3
4
5
6
7
t/τ_R (x 10^{-2})
10^{-8}
10^{-9}
10^{-10}
10^{-11}
m = 28, n = 12 MODE
3
4
5
6
7
t/τ_R (x 10^{-2})

Fig. 3

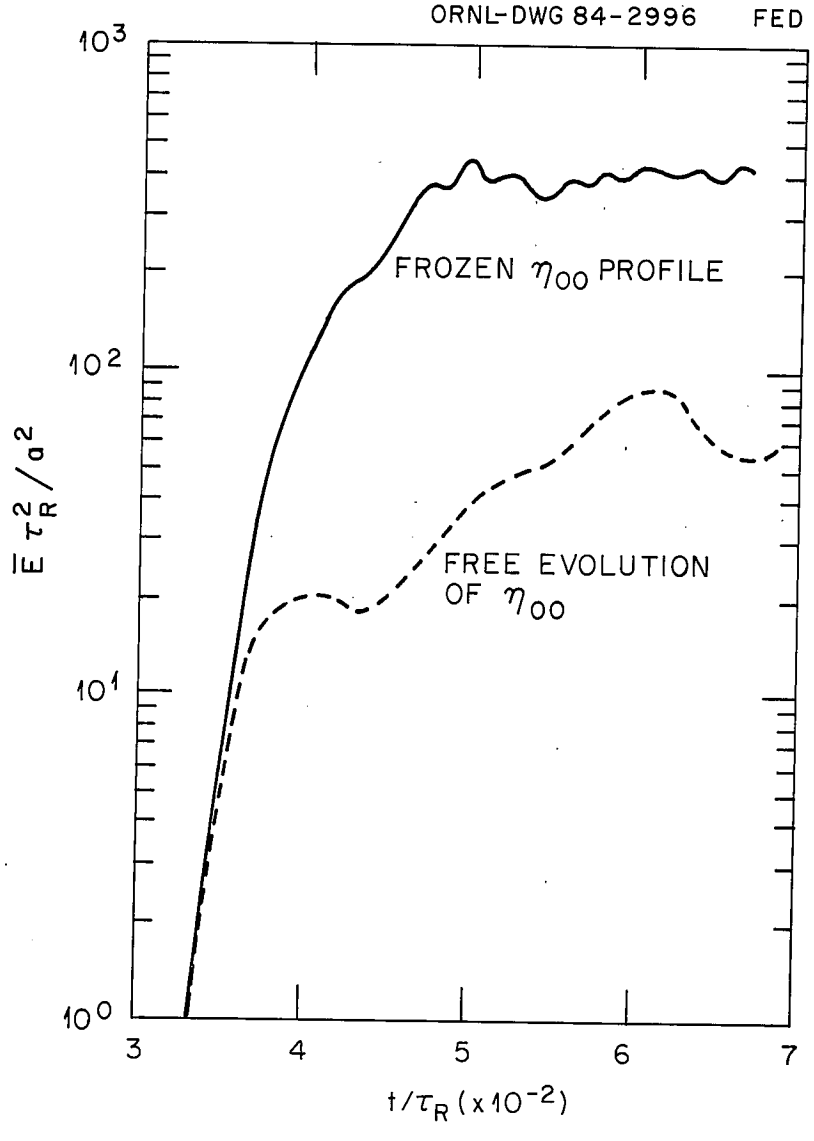
ORNL-DWG 84-2996 FED
10^3
10^2
10^1
10^0
$\bar{E}\tau_R^2/a^2$
FROZEN η_{00} PROFILE
FREE EVOLUTION OF η_{00}
3
4
5
6
7
t/τ_R ($\times 10^{-2}$)

Fig. 4

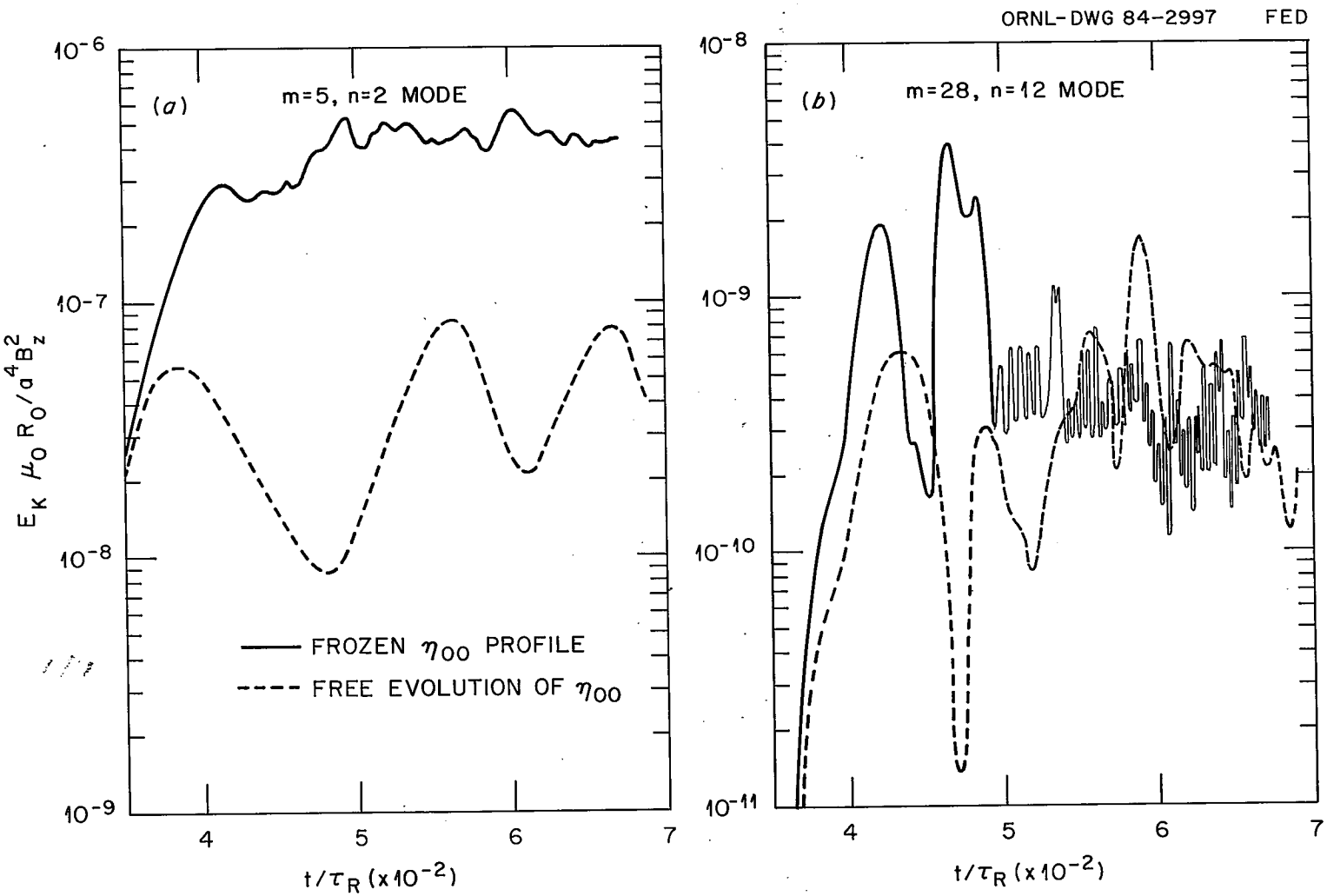
ORNL-DWG 84-2997 FED
(a)
m=5, n=2 MODE
(b)
m=28, n=12 MODE
$E_K \mu_0 R_0 / a^4 B_z^2$
FROZEN η_{00} PROFILE
FREE EVOLUTION OF η_{00}
t/τ_R (x10^{-2})
t/τ_R (x10^{-2})

Fig. 5

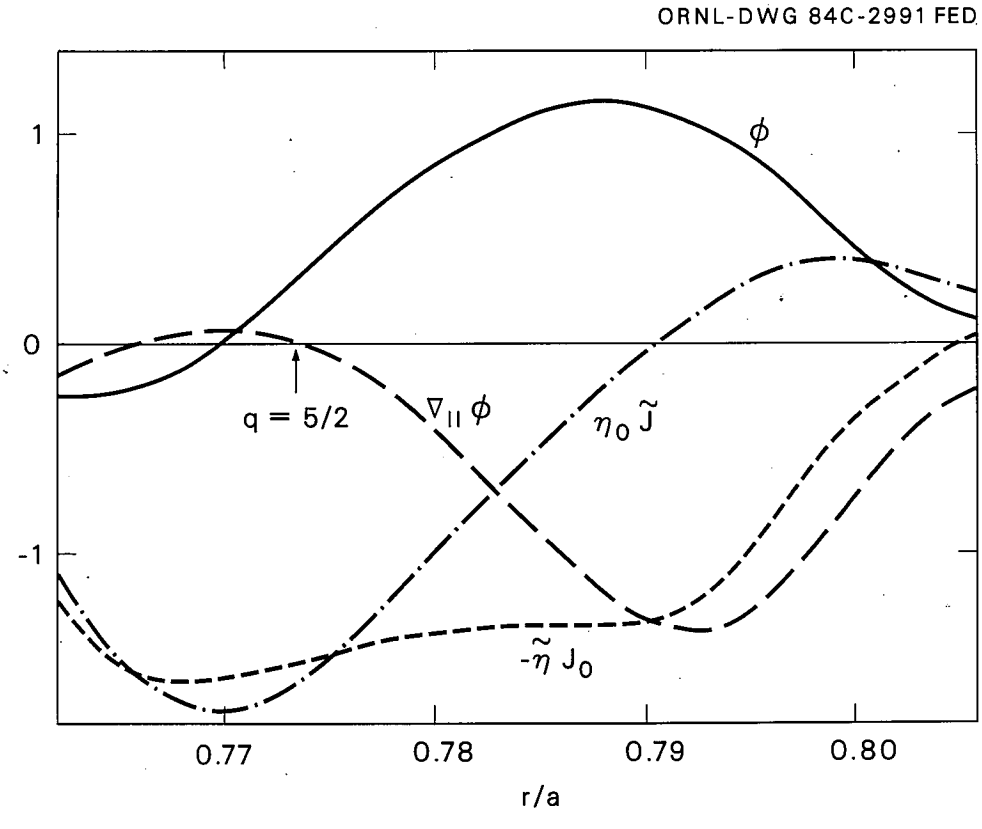
ORNL-DWG 84C-2991 FED
1
0
-1
ϕ
q = 5/2
$\nabla_{\parallel}\phi$
$\eta_0 \tilde{J}$
$-\tilde{\eta} J_0$
0.77
0.78
0.79
0.80
r/a

Fig. 6

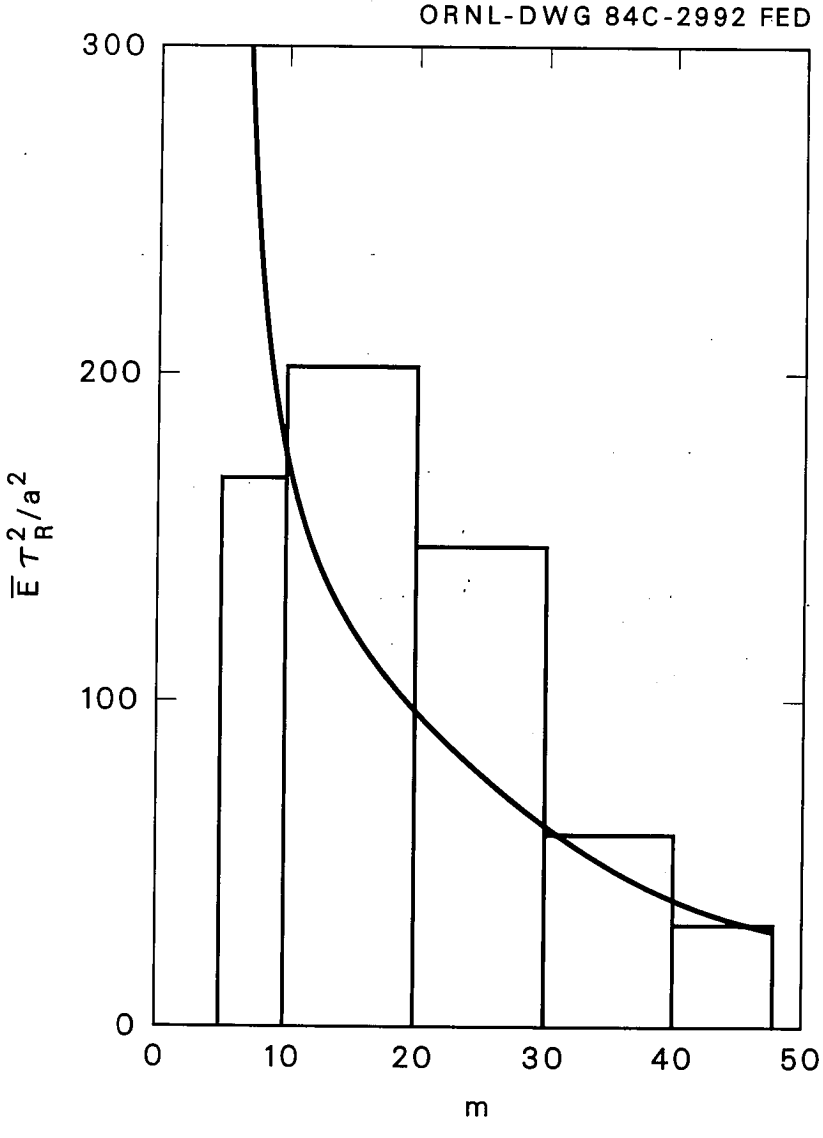
ORNL-DWG 84C-2992 FED
300
200
100
0
$\bar{E}\tau_R^2/a^2$
0
10
20
30
40
50
m

Fig. 7

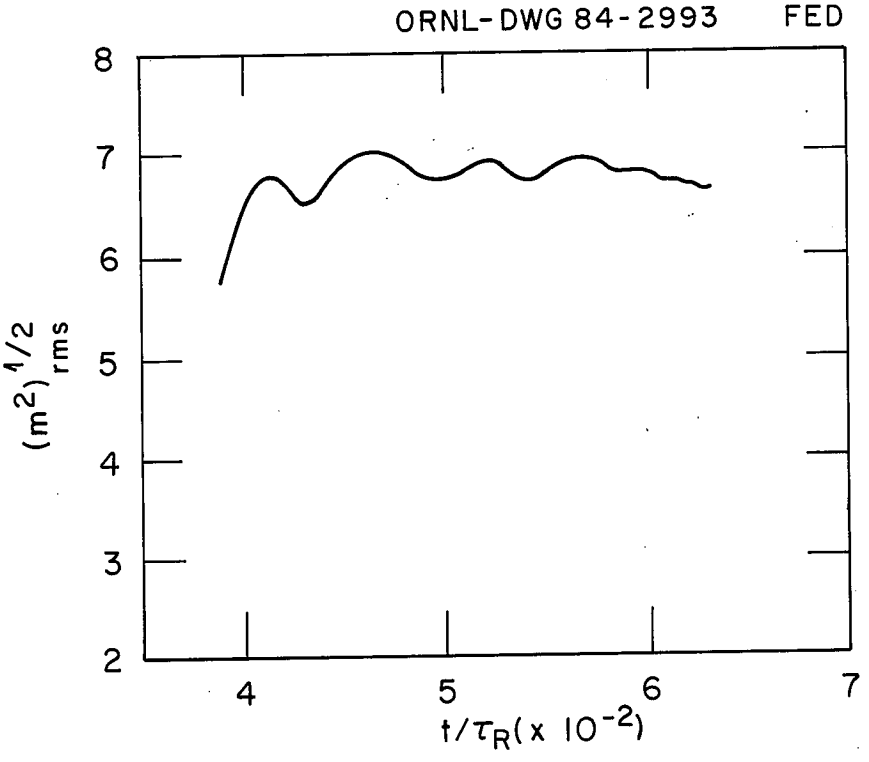

Fig. 3

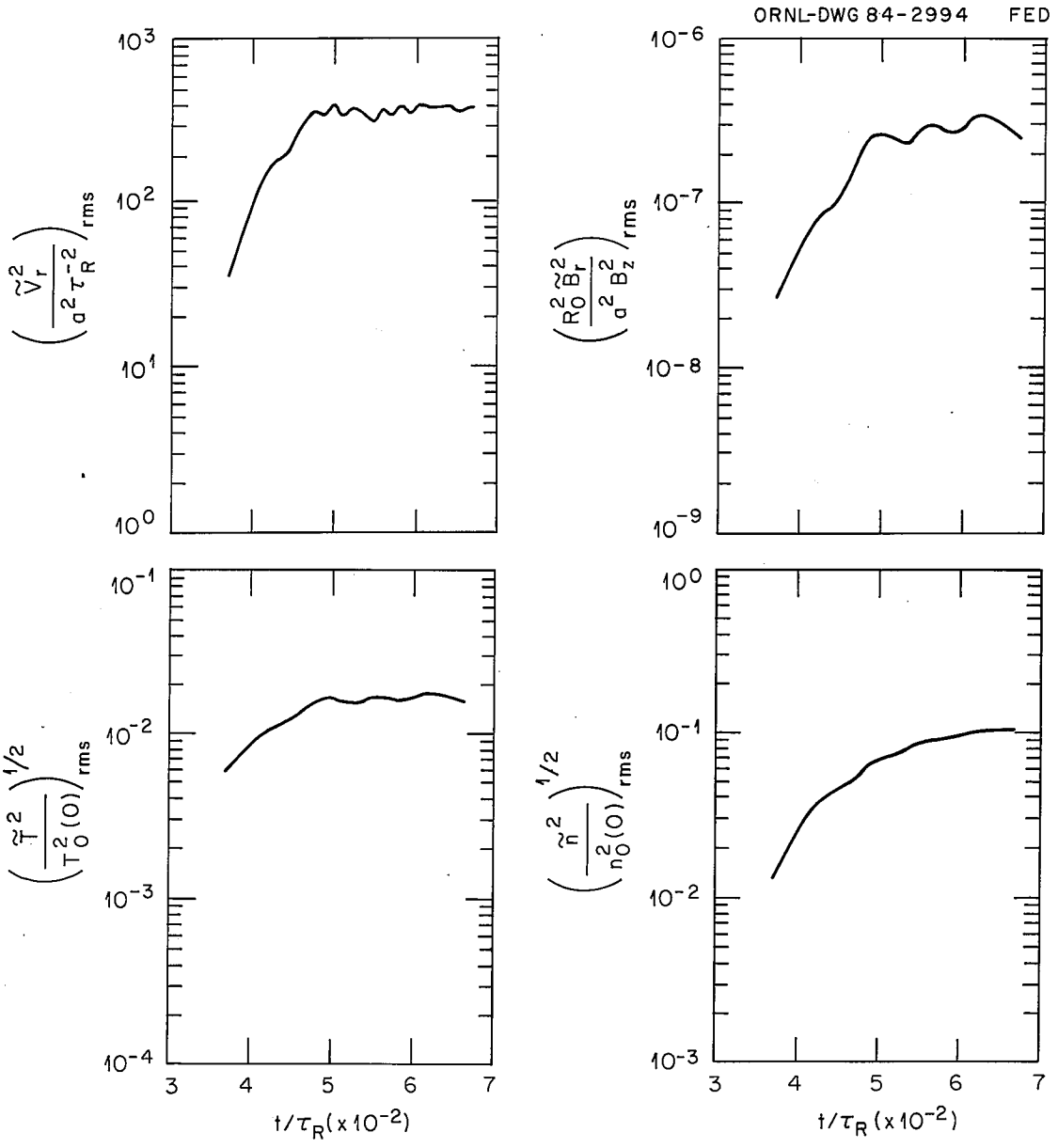
ORNL-DWG 84-2994 FED
$\left(\frac{\tilde{V}_r^2}{a^2\tau_R^{-2}}\right)_{rms}$
$\left(\frac{R_0^2\tilde{B}_r^2}{a^2B_z^2}\right)_{rms}$
$\left(\frac{\tilde{T}^2}{T_0^2(0)}\right)^{1/2}_{rms}$
$\left(\frac{\tilde{n}^2}{n_0^2(0)}\right)^{1/2}_{rms}$
$t/\tau_R (x10^{-2})$
$t/\tau_R (x10^{-2})$

Fig. 9

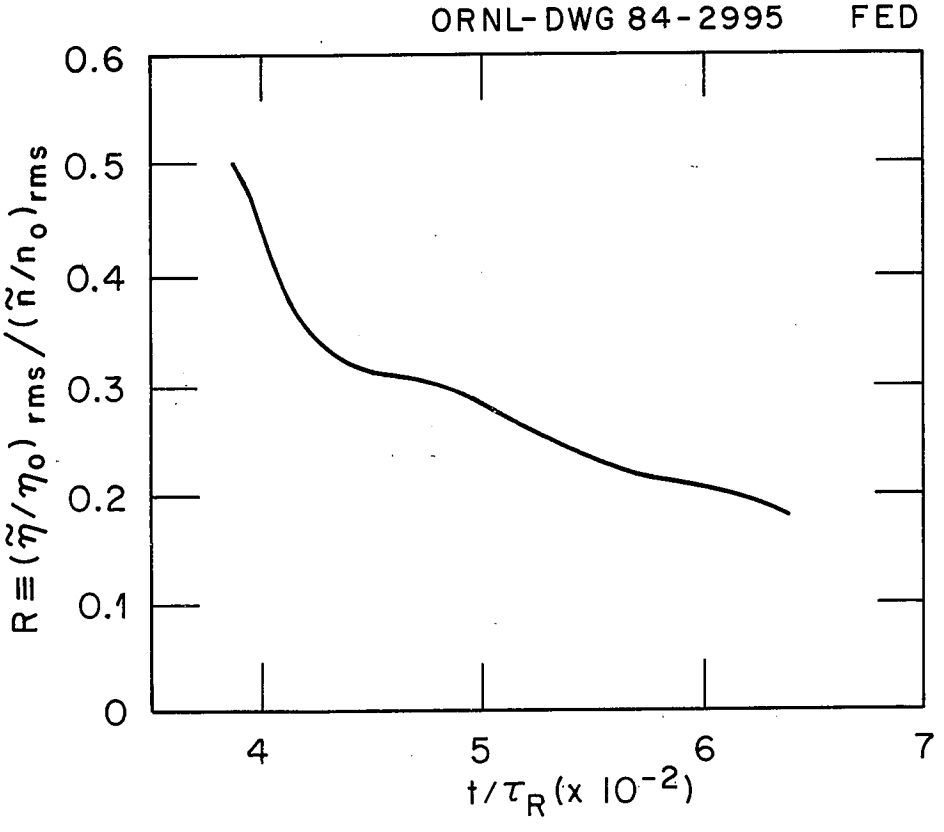
ORNL-DWG 84-2995 FED
0.6
0.5
0.4
0.3
0.2
0.1
0
4
5
6
7
$R \equiv (\tilde{\eta}/\eta_o)_{rms} / (\tilde{n}/n_o)_{rms}$
$t/\tau_R (x\ 10^{-2})$

Fig. 10